

Supplementary Information

A Dramatic Conformational Effect of Multifunctional Zwitterions on Zeolite Crystallization

Lei Dong,^{†,a} Dong Zhai,^{†,b} Zhuwen Chen,^a Guangchao Zheng,^a Yanding Wang,^a Mei Hong,^{*,a} Shihe Yang^{*,a}

[‡]State Key Laboratory of Chemical Oncogenomics, Guangdong Provincial Key Laboratory of Nano-Micro Materials Research, School of Chemical Biology & Biotechnology, Peking University Shenzhen Graduate School (PKUSZ), Shenzhen 518055, P.R. China.

[#]Institute of Molecular Sciences and Engineering, Shandong University, No.72 Binhai Road, Qingdao 266237, P.R. China.

*Corresponding Authors: hongmei@pku.edu.cn (M. Hong); chsyang@pku.edu.cn (S. Yang)

Experimental Methods

Materials: All reagents were of analytical grade and used as purchased without further purification. Sodium hydroxide were purchased from Sigma-Aldrich, sodium aluminate from General-Reagent, and Ludox (25% aqueous solution) from Qingdao Ocean Co., Ltd. *L*-carnitine and acetyl-*L*-carnitine hydrochloride were obtained from Energy Chemical and Adamas-beta respectively.

Synthesis of LTA Zeolites and in-situ Raman monitoring: LTA zeolites were synthesized according to our previous procedure.¹ To better monitor the crystallization kinetics and understand the role of organic small molecules, we employed a laser Raman spectrometer (Mettler Toledo ReactRaman 785) to monitor the entire crystallization process *in situ*. Before dosing in organic additives, the zeolite sol-gel was pre-aged and heated. In a typical LTA synthesis, 12.54 ml Ludox (25%) were dissolved in 20 ml deionized water within a three-necked flask, followed by a peristaltic pump addition of a clear solution containing 2.4 g NaOH and 4.92 g NaAlO₂ dissolved in 34 ml deionized water. After stirring at room temperature for 3 h, the solution was heated to 80 °C. For the synthesis in the presence of organics, e.g. *L*-carnitine, a solution containing 4.8 g *L*-carnitine in 5 ml deionized water was then dosed in at the same time. The resulting gel underwent crystallization at 100 °C for 20 h under constant stirring, meanwhile the ReactRaman sensor was directly placed in the synthesis system to monitor the crystallization process. The pH of the synthesis solution was monitored with a pH electrode (Mettler Toledo, FE20), which showed an alkaline reaction condition having pH between 13-14. The time-resolved or the product powder samples were collected by a refrigerated centrifuge, and dried at 60 °C for more than 12 h, named as MLTA-LC-unwashed. Some MLTA-LC-unwashed products were washed with deionized water until pH of the supernatant solution was close to 7, and dried at 60 °C for more than 12 h, designated as MLTA-LC-washed. The LTA-AcLC samples were synthesized in the same way except that equimolar of AcLC instead of LC was dosed after heated to 80 °C.

Characterization: Powder X-ray diffraction (XRD) patterns of zeolite was recorded using a Rigaku D/Max-2200 PC diffractometer in the diffraction angle range $2\theta = 4\text{--}50^\circ$ with Cu K α radiation ($\lambda = 1.5418 \text{ \AA}$) at 40 KV, 40 mA. Si/Al ratios of as synthesized samples were measured by energy dispersive X-ray analyser (EDX, Oxford, X-Max20 AZtec Energy 250, model no. XMX1112) and inductively coupled plasma-atomic emission spectroscopy (ICP-AES, Arcos II MV). Scanning electron microscope (SEM) was performed on a JEOL JSM-7800F electron microscope operated at 5.0 kV. The transmission electron microscopy (TEM) was performed on a Tecnai G2 F30 field emission source transmission electron microscope operated at 300 kV. The zeolite samples were ultramicrotomed to a thickness of 90 nm for TEM measurement after being embedded in a spurr epoxy resin. Centrifugation of suspension samples were conducted by a refrigerated centrifuge (Thermo Scientific - Fiberlite F21s-8x50y). Nitrogen adsorption-desorption isotherms were measured at -196 °C on a Micromeritics Tristar II 3020 v1.03 analyzer. The powder samples were degassed at 300 °C for at least 12 h before measurements. Fourier Transform infrared spectra were recorded in KBr pellets on a Shimadzu IR-Prestige 21 Spectrophotometer. In-situ Raman measurements were performed on a laser Raman spectrometer (Mettler Toledo ReactRaman 785) with a laser excitation wavelength of 785 nm. Ex-situ Raman measurements were performed on a laser Raman spectrometer (HORIBA LabRAM HR800) with a laser excitation wavelength of 532 nm (diode). For zeolite and zeolite containing samples, the *ex-situ* Raman measurements were carried out by focusing the laser on the suspension liquid of zeolite or composite samples. ²⁷Al Solid State Nuclear Magnetic Resonance (²⁷Al MAS NMR) were performed on a Bruker AVANCE III 600 spectrometer at a resonance frequency of 156.4 MHz. The ²⁷Al MAS NMR spectra were recorded on a 4 mm probe by small flip angle technique with a pulse length of 0.5 μs ($<\pi/12$), a 1s recycle delay and a spinning rate of 12 kHz. The chemical shifts were referenced to 1 mol/L aqueous Al(NO₃)₃ solution. Thermogravimetric analyses (TGA) were performed on a Shimadzu TGA-50 analyzer.

DFT Calculations: All the DFT calculations were carried out with Gaussian 16, C.01 program package². The initial atomic coordinates of LTA zeolite structure were taken from the International Zeolite Association (IZA). To represent (100) and (110) surfaces

of LTA zeolites, we constructed 24T cluster models containing 24 SiO₄ tetrahedron units cutting from the (100) and (110) surface slabs of the LTA zeolite, respectively. Except for different orientations, the cluster models for (100) and (110) surfaces both consist of half an LTA α -cage (Figure S12). We chose the most stable termination structures of the (100) and (110) surfaces according to Greñ et al.'s simulation study on LTA zeolite surfaces.³ The surface groups were terminated by OH groups. Dangling bonds of Si atoms at the edges of the cluster models were saturated with Si-H bonds. The bond lengths of the Si-H bonds were set to 1.56 Å. During the geometry optimization, all atoms in surface models were fixed except for the surface OH groups that were relaxed. To locate the most stable binding configurations of the LC and AcLC adsorbed on the zeolite surface models, we first searched many adsorption locations and configurations by simulated annealing using UFF force fields⁴. Then the structures with low energy were relaxed using DFT calculations at B3LYP-D3BJ/6-31G(d,p) level of theory⁵⁻⁸. To obtain more accurate energies, single-point calculations with larger basis sets 6-311++G(d,p) were performed for each relaxed structure. Solvent effects were included using the integral equation formalism variant of the polarizable continuum model (PCM) model⁹ with the dielectric constant of water in all DFT calculations.

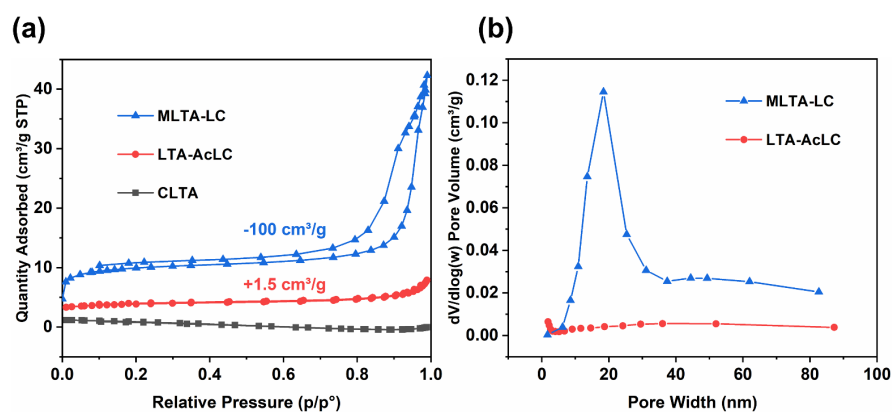


Fig. S1 (a) The N₂ adsorption-desorption isotherm and (b) BJH pore size distribution of as-synthesized samples. The negligible adsorption amount of nitrogen at 77 K for CLTA and LTA-AcLC samples indicate the solely microporous diffusion system <0.45 nm as the inherent LTA micropores of 0.41 nm pose severe kinetic restrictions at cryogenic temperature.¹⁰ The BJH pore size distribution for CLTA cannot be obtained due to the extremely low N₂ adsorption amount.

Table S1 Textural and compositional properties of as-obtained LTA samples.

Sample	S_{BET}^a ($\text{m}^2 \text{g}^{-1}$)	d_{meso}^b (nm)	V_{total}^c	V_{meso}^d	Si/Al ^e
CLTA	N.O. ^f	N.O.	N.O.	N.O.	1.02
LTA-AcLC	1.5	N.O.	N.O.	N.O.	1.06
MLTA-LC	90	18.4	0.09	0.05	1.11

^a The BET surface area (S_{BET}) calculated from N₂ adsorption isotherm in a relative pressure range of 0.05–0.30. ^b Mesopore diameter (d_{meso}) obtained from the desorption branch using the BJH method. ^c Total pore volume (V_{total}) calculated as the amount of N₂ adsorbed at $P/P_0 = 0.98$. ^d Mesopore volume (V_{meso}) calculated as (total pore volume – V_{mic} obtained from a t -plot method). ^e Si/Al ratios of the as synthesized samples measured using inductively coupled plasma-atomic emission spectroscopy (ICP-AES). ^f N.O. Data cannot be explicitly obtained as the N₂ molecules with larger size can hardly access the micropore in NaA. All samples were degassed at 300 °C for at least 12 h.

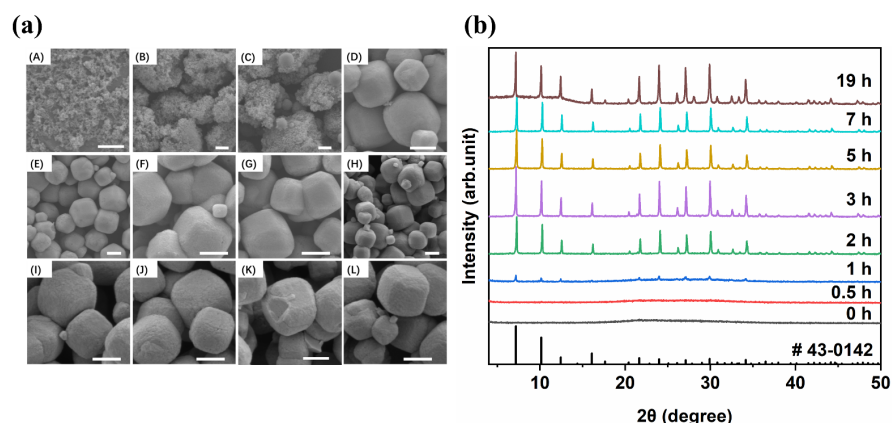


Fig. S2 The fast crystallization of organic-free NaA (CLTA) zeolite synthesis. (a) SEM images of zeolite CLTA samples at different growth stages, scale bar represents 1 μm ; (b) XRD patterns of CLTA samples evolved at different growth stages.

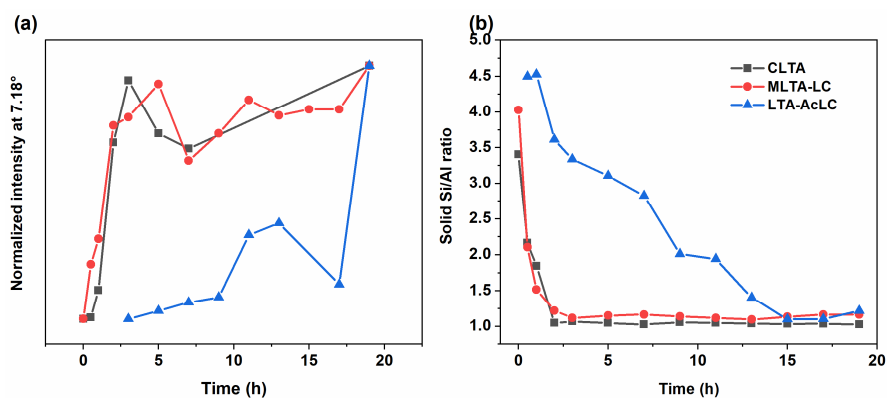


Fig. S3 (a) Plot of normalized XRD peak intensity at $2\theta=7.18^\circ$ as a function of hydrothermal synthesis time with the peak intensity at 19 h assumed to be 100%, and (b) Si/Al ratios of the solid samples collected at various crystallization time of MLTA-LC, CLTA and LTA-AcLC.

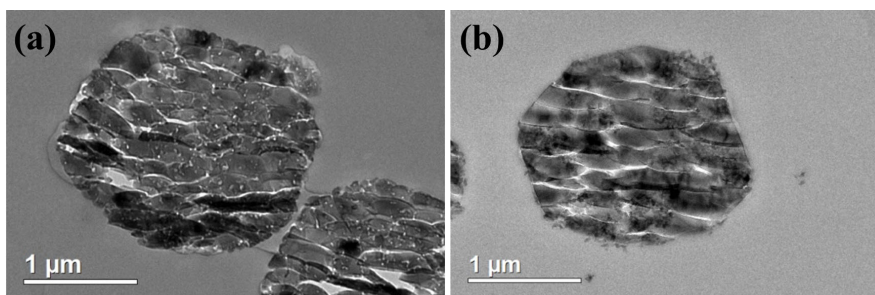


Fig. S4 Low-resolution TEM images of as-synthesized (a) MLTA-LC and (b) LTA-AcLC samples confirming the mesopore function of LC and crystal modifier function of AcLC. All the samples were hydrothermally synthesized for 19 h, washed and dried before ultrathin sectioning.

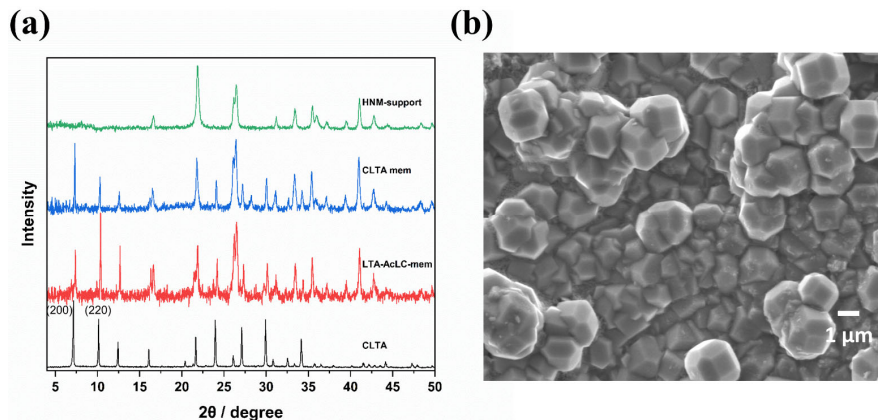


Fig. S5 (a) Comparative XRD patterns of LTA-AcLC membranes in comparison with CLTA membranes prepared according to our previous report¹¹ as well as the support of halloysite nanotube-based mats (HNM) and LTA seed used for the membrane synthesis; (b) surface SEM image of the as-synthesized LTA-AcLC membrane showing obvious dodecahedron shape of the zeolite crystals with a mixture of {100} and {110} facets.

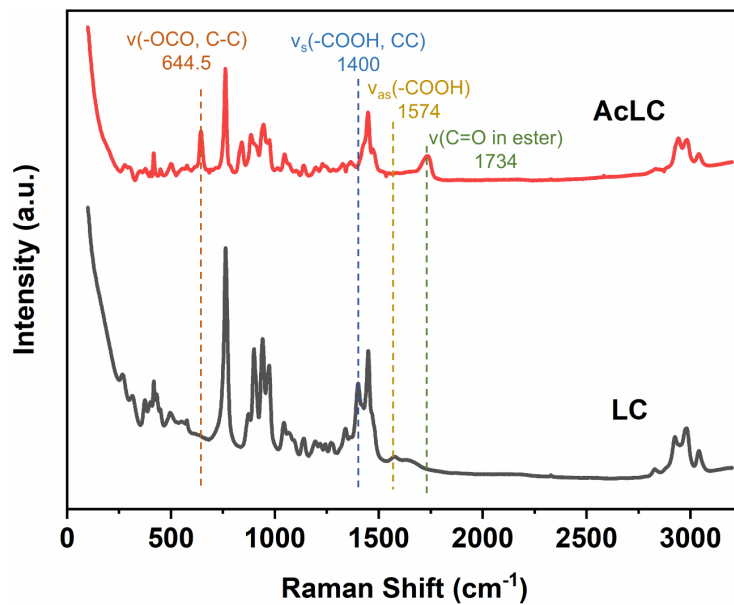


Fig. S6 Comparative ReactRaman spectra of aqueous solution of LC and AcLC.

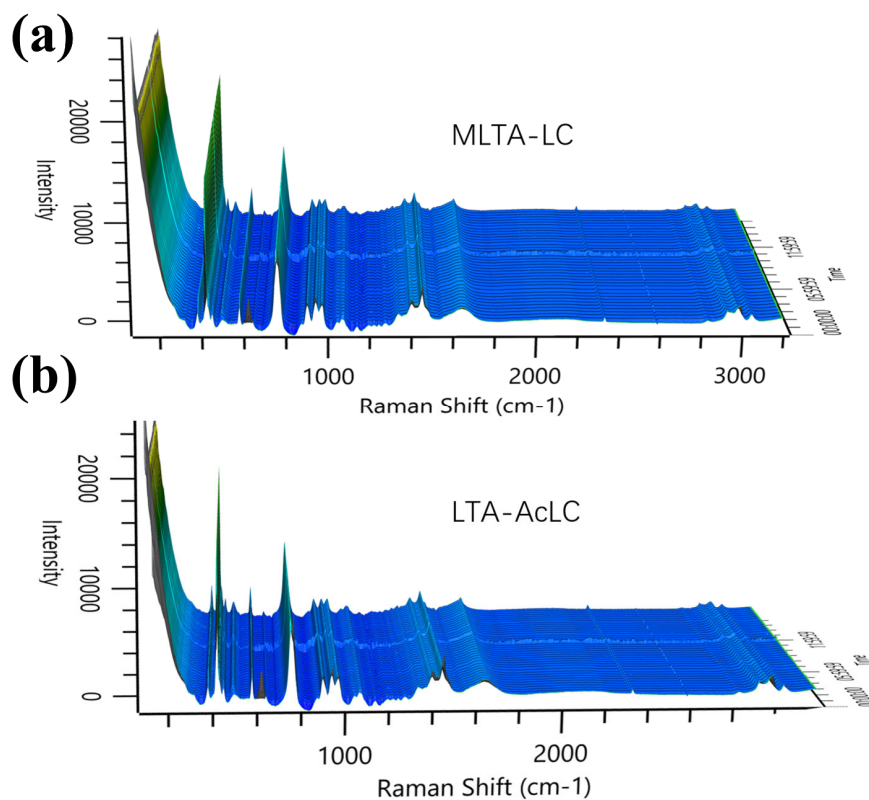


Fig. S7 ReactRaman spectra in the full wavelength between 0-3200 cm^{-1} of LTA crystallization with additives of (a) LC and (b) AcLC.

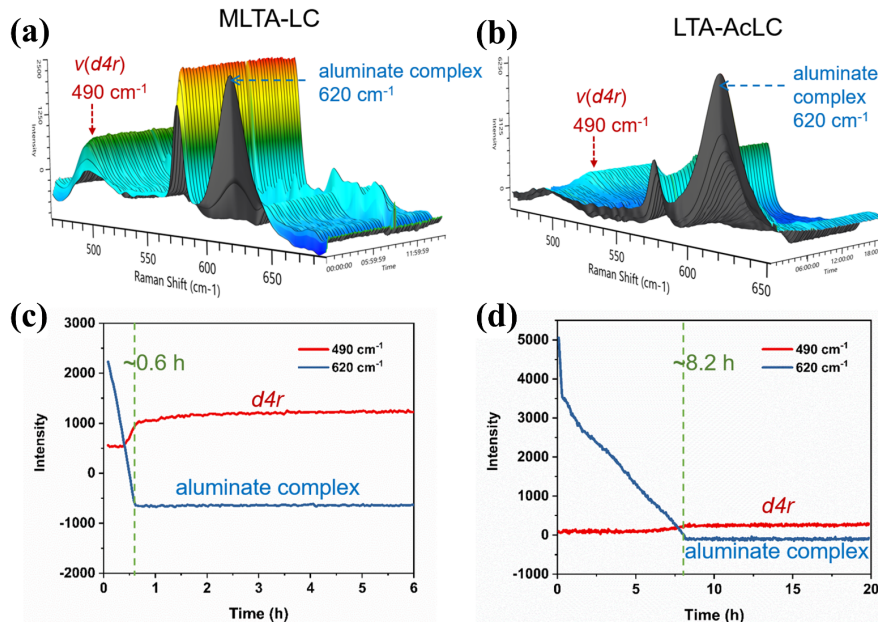


Fig. S8 Comparative ReactRaman results of LTA synthesis system showing great zeolite growth inhibition effect of acetylcarnitine. (a-b) Time-resolved in-situ Raman spectra between $\sim 450\text{--}700\text{ cm}^{-1}$ of the (a) MLTA-LC and (b) LTA-AcLC synthesis system, and the corresponding intensity profile of 490 and 620 cm^{-1} peaks representing LTA *d4r* unit and precursor aluminate complex.

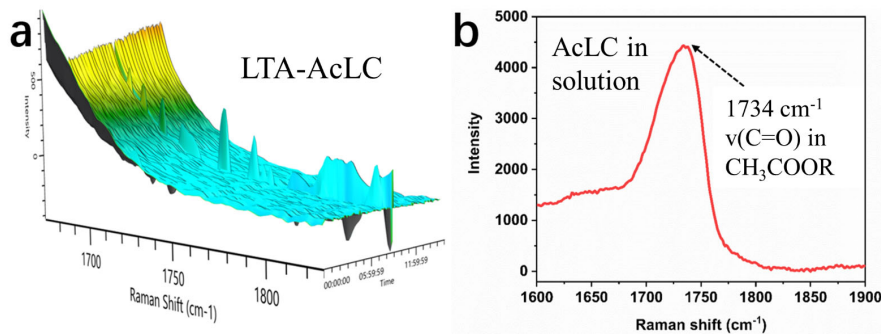


Fig. S9 Comparative ReactRaman results of (a) LTA-AcLC synthesis system and (b) pure AcLC aqueous solution showing disappearance of the stretching vibration peak of the acetyl carbonyl group from AcLC when added into the LTA zeolite synthesis system.

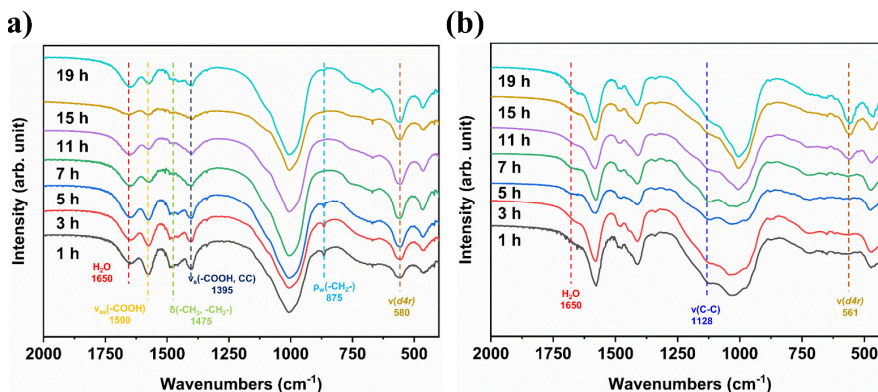


Fig. S10 Comparative FTIR spectra of (a) MLTA-LC, (b) LTA-AcLC samples at different growth stages showing retarded crystallization and more intense hydrophobic interactions caused by AcLC addition into the LTA zeolitization system. All the samples were centrifuged, and the precipitates were collected for drying without a further water-washing step.

In the unwashed-MLTA-LC FTIR spectra (Fig. S10a), bending mode of adsorbed water molecule at 1650 cm^{-1} persist in all samples, confirming the strong hydrophilicity due to low Si/Al ratio. The peaks ascribed to --COOH asymmetric stretching vibration¹² at 1590 cm^{-1} and symmetric stretching at 1395 cm^{-1} do not change much in intensity, while the peak of methyl and methylene group vibration and deformation at 1475 cm^{-1} become almost indiscernible after $t=7\text{ h}$. Supportively, the $\text{--CH}_2\text{--}$ wagging at 875 cm^{-1} , discernible for samples synthesized between 0-5 h, disappears from $t=7\text{ h}$ on. The hydrophobic methyl and methylene group in LC might be buried in the zeolite interior after LTA framework has been completely formed, avoiding exposure to the aqueous synthesis gel. A weak IR band at 580 cm^{-1} due to

$d4r$ unit¹³ is detectable in products upon $t=0$ h and becomes obvious at $t=3$ h. On the contrary, in LTA-AcLC unwashed samples (Fig. S10b), water bending mode around 1650 cm^{-1} can hardly be seen during all reaction time, clearly illustrating the loss of induced transition dipole moment caused by capping effect of AcLC and its induced shape change of LTA crystals.¹⁴

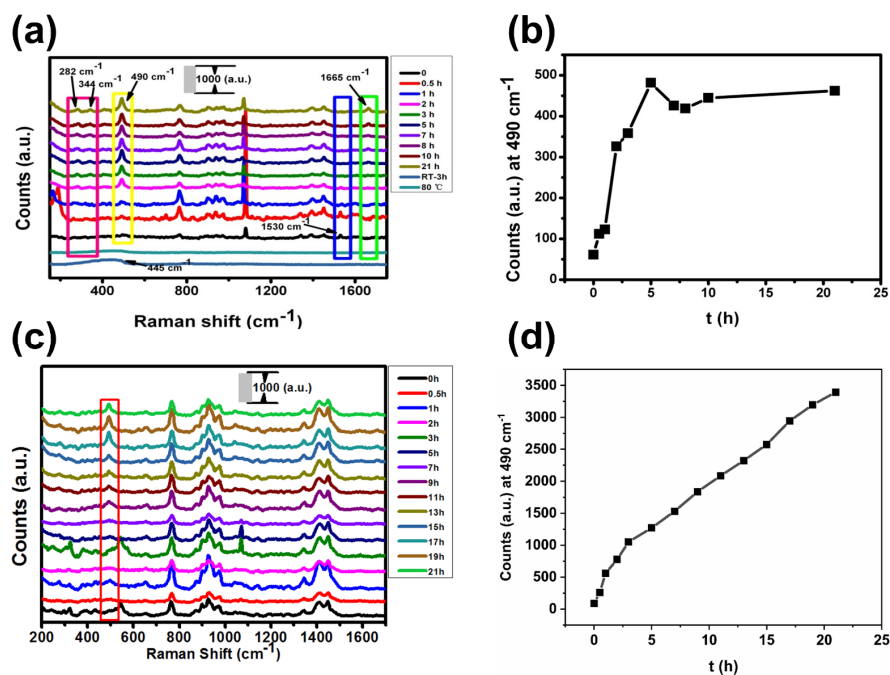


Fig. S11 (a) Evolution of Raman spectra of MLTA-LC system during hydrothermal synthesis, (b) plot of Raman intensity at 490 cm^{-1} of MLTA-LC system as a function of hydrothermal synthesis time and (c) evolution of Raman spectra of LTA-AcLC system during hydrothermal synthesis, (d) plot of Raman intensity at 490 cm^{-1} of LTA-AcLC system as a function of hydrothermal synthesis time. All the samples were centrifuged, and the precipitates were collected for drying without a further water-washing step.

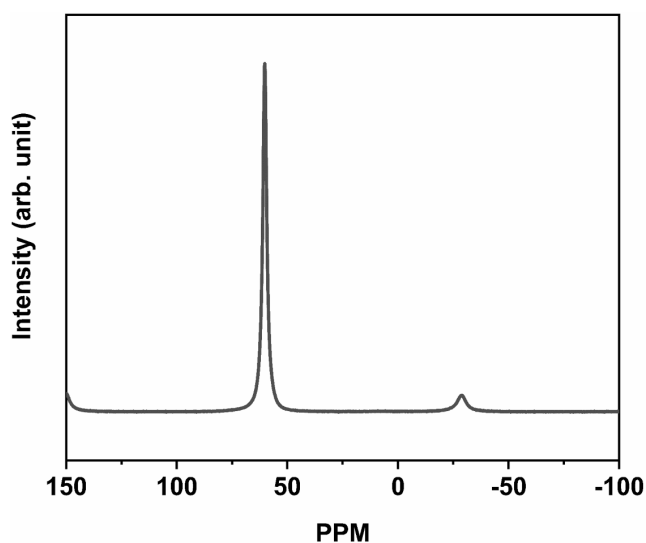


Fig. S12 ^{27}Al MAS NMR spectra of the as-synthesized CLTA sample.

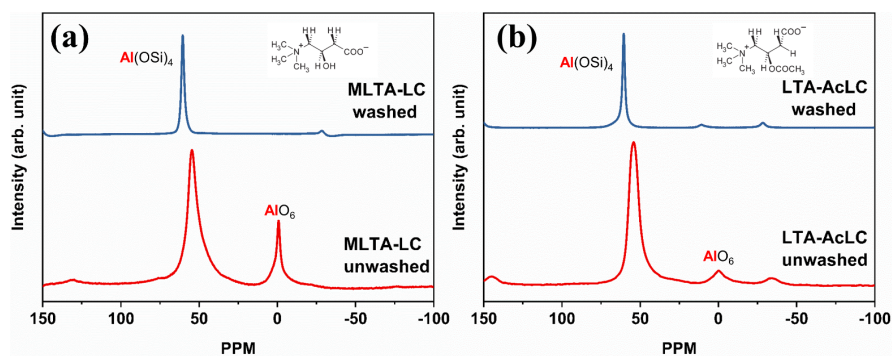


Fig. S13 ^{27}Al MAS NMR spectra of as-synthesized (a) MLTA-LC and (b) LTA-AcLC samples. All these samples were hydrothermally synthesized for 19 h.

Further investigate employing ^{27}Al solid-state MAS NMR measurements on CLTA (Fig. S12), MLTA-LC (Fig. S13a), and LTA-AcLC (Fig. S13b) showed that main signals for all samples are located at 50–70 ppm, assigned to tetrahedrally coordinated Al. For unwashed MLTA-LC samples, an obvious peak at about 0.66 ppm appears with much higher intensity than that of unwashed LTA-AcLC, suggesting octahedrally coordinated Al species extracted from the lattice by *in-situ* demetallation process through stronger coordination of framework Al by LC molecules.¹⁵ For the thoroughly washed MLTA-LC, only a sharp peak at 60.63 ppm and no peaks at 0–5 ppm can be found, indicating that the mesopores generated by LC are interconnected throughout the entire MLTA crystal, so that AlO_6 species can be easily removed by water wash. On the contrary, for unwashed LTA-AcLC, there is only a weak peak at 0.66 ppm confirming negligible coordination of Al to AcLC additives and this peak still remain in the washed LTA-AcLC sample probably due to diffusion limitation of the solely microporous system.

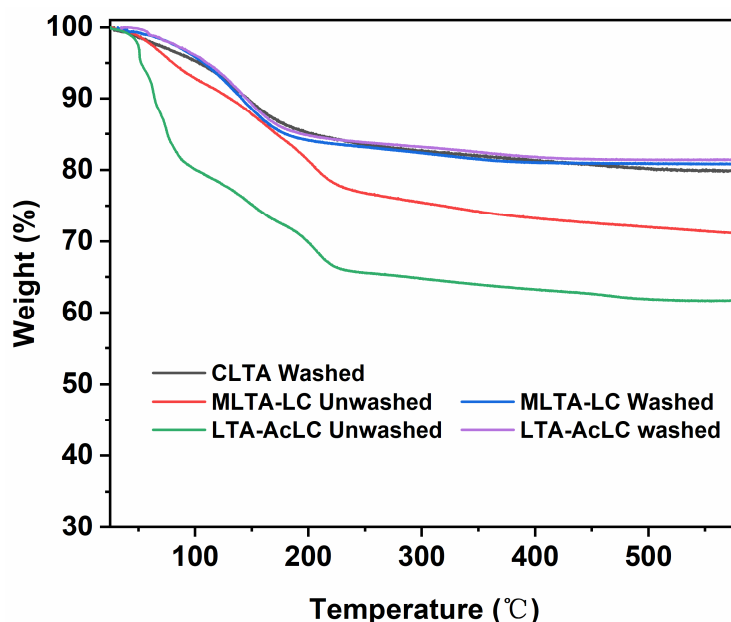


Fig. S14 TGA curve of as-synthesized samples. The washed MLTA-LC and LTA-AcLC samples are almost identical to that of washed CLTA samples synthesized without organics, indicating that water washing could remove almost all organics from product LTA probably due to high solubility of these zwitterions in water. The higher percentage of organics in unwashed LTA-AcLC than in the unwashed MLTA-LC is probably due to the higher molecular weight of AcLC.

From the TGA plots (Fig. S14), the unwashed MLTA-LC and LTA-AcLC both show organics incorporation in the LTA crystals with higher percentage in unwashed LTA-AcLC than in the unwashed MLTA-LC and complete organics removal by water washing. Therefore, the mesopore generation is based on chemical effect of LC, not the physical space-filling mechanism which requires energy-intensive calcination step.^{1,15}

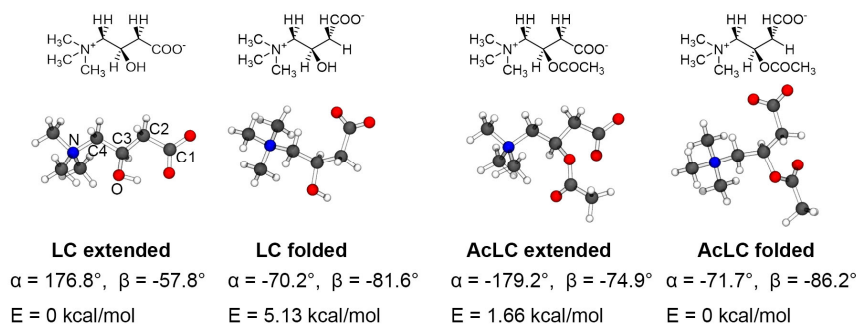


Fig. S15 Molecular structure of LC and AcLC and their solution state conformation.

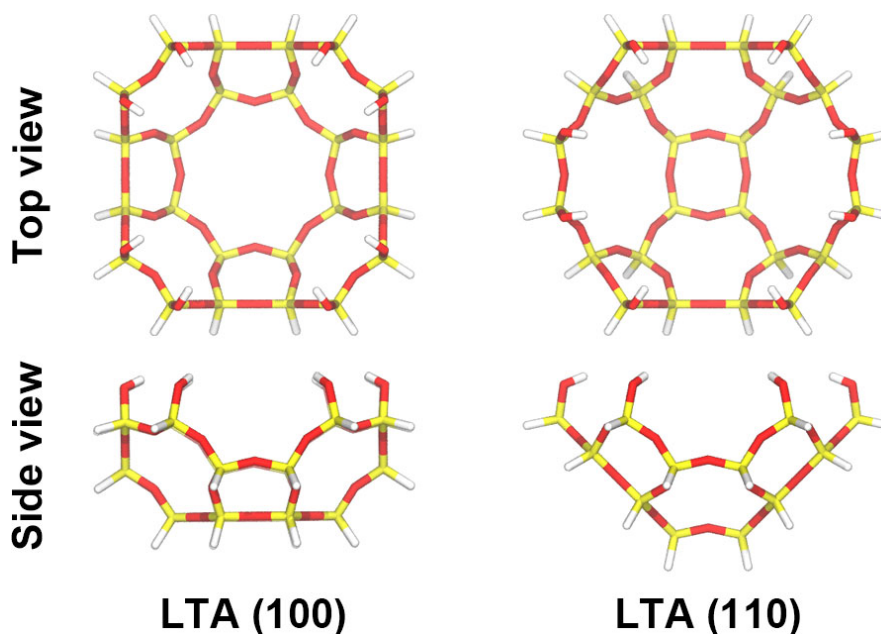


Fig. S16 Cluster models for LTA (100) and (110) surfaces.

REFERENCES

- 1 Z. Chen, J. Zhang, B. Yu, G. Zheng, J. Zhao and M. Hong, *J. Mater. Chem. A*, 2016, **4**, 2305-2313.
- 2 M. J. Frisch, G. W. Trucks, H. B. Schlegel, et al., Gaussian 16, Revision C.01; Gaussian, Inc.: Wallingford, CT, 2019.
- 3 W. Gren, S. C. Parker, B. Slater and D. W. Lewis, *J. Phys. Chem. C*, 2010, **114**, 9739-9747.
- 4 A. K. Rappé, C. J. Casewit, K. Colwell, W. A. Goddard III and W. M. Skiff, *J. Am. Chem. Soc.*, 1992, **114**, 10024-10035.
- 5 C. Lee, W. Yang and R. G. Parr, *Phys. Rev. B*, 1988, **37**, 785-789.
- 6 A. Becke, *J. Chem. Phys.*, 1993, **98**, 5648-5652.
- 7 P. J. Stephens, F. Devlin, C. Chabalowski and M. J. Frisch, *J. Phys. Chem.*, 1994, **98**, 11623-11627.
- 8 S. Grimme, J. Antony, S. Ehrlich and H. Krieg, *J. Chem. Phys.*, 2010, **132**, 154104-154122.
- 9 J. Tomasi, B. Mennucci and R. Cammi, *Chem. Rev.*, 2005, **105**, 2999-3094.
- 10 K. A. Cychoz, R. Guillet-Nicolas, J. García-Martínez and M. Thommes, *Chem. Soc. Rev.*, 2017, **46**, 389-414.
- 11 Z. Chen, J. Zeng, D. Lv, J. Gao, J. Zhang, S. Bai, R. Li, M. Hong and J. Wu, *R. Soc. Open Sci.*, 2016, **3**, 160552-160566.
- 12 E. Podstawka, M. Świątłowska, E. Borowiec and L. M. Proniewicz, *J. Raman Spectrosc.*, 2007, **38**, 356-363.
- 13 M. B. Park, Y. Lee, A. Zheng, F.-S. Xiao, C. P. Nicholas, G. J. Lewis and S. B. Hong, *J. Am. Chem. Soc.*, 2012, **135**, 2248-2255.
- 14 V. Crupi, F. Longo, D. Majolino and V. Venuti, *J. Phys.: Condens. Matter* 2006, **18**, 3563-3580.
- 15 C. Chen, D. Zhai, L. Dong, Y. Wang, J. Zhang, Y. Liu, Z. Chen, Y. Wang, W. Qian and M. Hong, *Chem. Mater.*, 2019, **31**, 1528-1536.